Control of magnetic anisotropy by epitaxial strain in the *n*-type ferromagnetic semiconductor (In,Fe)Sb

Akhil Pillai [1], Shobhit Goel [1], Le Duc Anh [1,2,3,*] and Masaaki Tanaka [1,3,4,†]

[1]*Department of Electrical Engineering and Information Systems, The University of Tokyo,
7-3-1 Hongo, Bunkyo-ku, Tokyo 113–8656, Japan*

[2]*PRESTO, Japan Science and Technology Agency, 4-1-8 Honcho, Kawaguchi, Saitama 332-0012, Japan*

[3]*Center for Spintronics Research Network (CSRN), The University of Tokyo, 7-3-1 Hongo, Bunkyo-ku, Tokyo 113–8656, Japan*

[4]*Institute for Nano Quantum Information Electronics (NanoQuine), The University of Tokyo,
4-6-1 Komaba, Meguro-ku, Tokyo 153-0041, Japan*

We report the strain dependence of magnetic anisotropy in *n*-type ferromagnetic semiconductor (FMS) (In,Fe)Sb thin films grown on different buffer layers; ranging from an InSb buffer layer that induces in-plane tensile strain, to AlSb, GaSb, and InAs buffer layers that induce an increasing order of in-plane compressive strain. Using ferromagnetic resonance (FMR) measurements and theoretical fittings, we show that the magnetocrystalline anisotropy constant (K_i) changes its sign, corresponding to a change in its preference for an in-plane magnetization easy axis to a perpendicular magnetization easy axis, when the epitaxial strain is changed from tensile to compressive. Meanwhile, the shape anisotropy constant (K_{sh}), which favors an in-plane magnetization easy axis, has larger contribution over K_i. Thus, the effective magnetic anisotropy ($K_{eff} = K_i + K_{sh}$) results in in-plane magnetic anisotropy in all our (In,Fe)Sb thin films. Our study presents the observation of FMR in the *n*-type FMS (In,Fe)Sb at different temperatures and under various strain conditions. We discuss the origin of the strain-dependent magnetization anisotropy of (In,Fe)Sb with the help of a band-structure model while taking $p - d$ hybridization into account.

I. INTRODUCTION

Ferromagnetic semiconductors (FMSs), exhibiting both the properties of ferromagnets and semiconductors, are an attractive choice of materials for developing semiconductor-based spintronics devices [1–3]. One of the major driving motivations is their good compatibility with the current semiconductor technology, particularly with the III-V semiconductor family. FMSs provide new functions that are difficult to realize in metallic ferromagnets such as electrical control of magnetization [3] and band engineering of magnetic structures to form *p-n* junctions or low-dimensional quantum structures [2]. FMSs are also potentially better candidates than their metallic counterparts for performing spin injection into semiconductor channels without suffering from the problem of conductivity mismatch [4]. This advantage omits the necessity of introducing a tunnel barrier at the FMS/semiconductor interface, and thus lowers the parasitic resistances, promisingly leading to higher spin-valve magnetoresistance in spin-based metal-oxide-semiconductor field-effect transistors [5].

For about two decades, there have been extensive studies on the various properties of Mn-doped FMSs, especially prototypical (Ga,Mn)As [6–8], from new devices such as spin diodes [9,10], magnetic tunnel junctions [11,12], planar Hall-effect devices [13], to new functionalities such as spin pumping [14] and electrical spin injection [15–18]. However, (In,Mn)As and (Ga,Mn)As exhibit low Curie temperature ($T_C \sim 90$ K [19] and 200 K [20], respectively) and only *p*-type carriers. These drawbacks significantly hinder the applications of these Mn-doped FMSs, especially those to be used at room temperature.

To solve these problems, a new family of III-V ferromagnetic semiconductors wherein iron (Fe) is used as the magnetic dopant has been developed [21–32]. These materials include *p*-type (Ga,Fe)Sb [21,22,24,27], *n*-type (In,Fe)Sb [23,24,26,27,29], *n*-type (In,Fe)As [24,25,30,31], and insulating (Al,Fe)Sb [28]. (Ga,Fe)Sb and (In,Fe)Sb exhibit T_C as high as 340 K [22] and 385 K [29], respectively, while (In,Fe)As thin films grown on off-cut substrates also show ferromagnetism above room temperature (300 K) [33]. (In,Fe)As is the first *n*-type FMS where a large spontaneous spin-splitting energy (30–50 meV) in the conduction band has been observed [31,32]. Therefore, these Fe-doped FMSs can potentially overcome the long-standing problems in FMSs, paving ways towards practical semiconductor-based spintronics devices.

With new FMSs available, it is imperative to clarify their magnetic anisotropy for fundamental understanding and device applications. Magnetic anisotropy is a crucial parameter of a ferromagnetic material to minimize the power consumption in fundamental operations including magnetization

*anh@cryst.t.u-tokyo.ac.jp
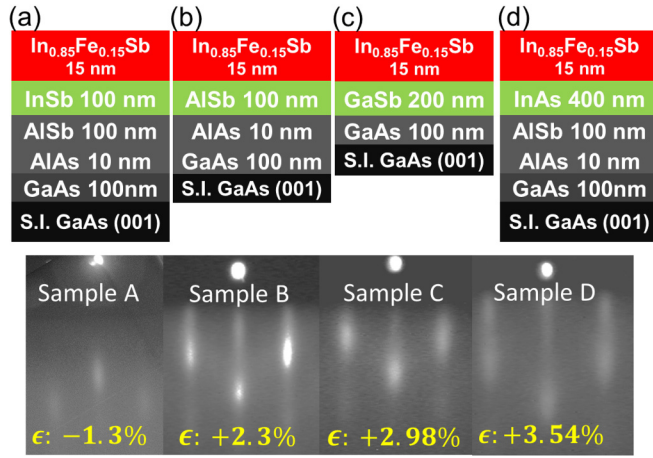†masaaki@ee.t.u-tokyo.ac.jp

FIG. 1. (Top view) (a)–(d) Schematic sample structures of $(In_{0.85}, Fe_{0.15})Sb$ grown on different buffer layers on semi-insulating GaAs(001) substrates. (Bottom view) *In situ* reflection high-energy electron diffraction (RHEED) patterns observed along the $[\bar{1}10]$ axis of the (In,Fe)Sb thin films, together with the corresponding strain values ε, are shown. Positive (negative) ε values indicate compressive (tensile) strain induced in the ferromagnetic (In,Fe)Sb films.
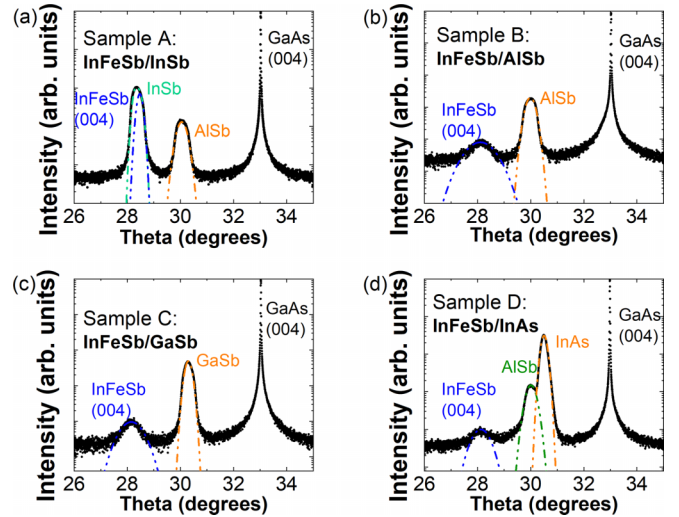

FIG. 2. (a)–(d) X-ray diffraction curves ($\omega - 2\theta$ scans) of samples A–D. The blue dotted line (Gaussian fitting) indicates the peak of (In,Fe)Sb. Other colored lines (Gaussian fitting) indicate the peaks of InSb, AlSb, GaSb, and InAs buffer layers. All samples were grown on semi-insulating GaAs substrates.

reversal. Spintronics devices, such as magnetic tunnel junctions [34–37], spin diodes [38,39], and spin transistors [40,41], require FMSs with magnetic anisotropy that is both strong, for maintaining stable magnetized orientations, and highly controllable, for implementing efficient magnetization switching. In the past, the magnetic anisotropy of Mn-doped FMSs [42–51] was studied intensively by varying the strain and the hole concentration. For Fe-doped FMSs, studies on the magnetic anisotropy of *p*-type (Ga,Fe)Sb [52–54] were reported recently. However, there has been no such study for *n*-type FMSs, except for Ref. [29], which was not comprehensive. It is expected that *n*-type FMSs exhibit weaker magnetic anisotropy than their *p*-type counterparts because the conduction band is generally more isotropic than the valence band. In this paper, we report the systematic investigation of the magnetic anisotropy of an *n*-type FMS, (In,Fe)Sb (Fe concentration: 15%, $T_C = 260 - 310$ K), at high temperatures (300 and 150 K). We study the effect of epitaxial strain on the magnetic anisotropy of (In,Fe)Sb using ferromagnetic resonance (FMR) measurements, and determine the anisotropy constants.

II. SAMPLE GROWTH AND CHARACTERIZATION

We grew four samples, namely sample A–D, of *n*-type FMS $(In_{0.85}, Fe_{0.15})Sb$ with an Fe concentration fixed at 15% on semi-insulating (S.I.) GaAs(001) substrates by low-temperature molecular-beam epitaxy (LT-MBE). As shown in Figs. 1(a)–1(d), the samples A–D comprise a 15-nm-thick (In,Fe)Sb thin film grown on four types of buffer layers: InSb, AlSb, GaSb, and InAs, respectively, which induce in-plane tensile strain (InSb) and compressive strain (AlSb, GaSb, and InAs) to the (In,Fe)Sb films.

In all the samples, we first grew a 100-nm-thick GaAs layer on S.I. GaAs substrate at a substrate temperature $T_S = 550°$ C. After that, for samples A, B, and D we grew a 10-nm-thick

AlAs layer at the same T_S. Next, we grew a 100-nm-thick AlSb layer at $T_S = 470°$ C. For sample A (D), we grew a 100-nm-thick InSb layer at $T_S = 400°$ C (400-nm-thick InAs at $T_S = 470°$ C for sample D) on top of the AlSb layer. For sample C, after the growth of GaAs, a 200-nm-thick GaSb layer was grown directly on GaAs at $T_S = 470°$ C. Finally, a 15-nm-thick $(In_{0.85}, Fe_{0.15})Sb$ layer was grown on the top of the buffer layers with a growth rate of 0.5 μm/h at $T_S = 240°$ C. The growth process was monitored *in situ* using reflection high-energy electron diffraction (RHEED), which is shown in the lower panels of Figs 1(a)–1(d). The (In,Fe)Sb thin films show relatively bright and streaky RHEED patterns, thereby indicating good two-dimensional growth of zinc-blende crystal structures in all the samples.

Next, we estimated the lattice constants of the (In,Fe)Sb layers in samples A–D by using $\omega - 2\theta$ measurements of x-ray diffraction (XRD), whose results are plotted in Figs. 2(a)–2(d). All the samples show a sharp GaAs (004) peak and an AlSb (004) peak (except sample C). In samples B, C, and D, the (In,Fe)Sb (004) peak is clearly visible, while in sample A, there is a broad peak comprising both the (In,Fe)Sb (004) peak and the InSb (004) peak. From the peak positions, we estimated the intrinsic lattice constants of (In,Fe)Sb (a_{InFeSb}) and of the buffer layer (a_{buffer}) (see Sec. 1 in Supplemental Material [55]). We defined the epitaxial strain as $\varepsilon = \frac{a_{InFeSb} - a_{buffer}}{a_{InFeSb}} \times 100$ (%). The XRD results indicated compressive strain in sample B (AlSb, $\varepsilon : +2.3\%$), C (GaSb, $\varepsilon : +2.98\%$), and D (InAs, $\varepsilon : +3.54\%$), and tensile strain in sample A (InSb, $\varepsilon : -1.3\%$). Thus, we can vary the epitaxial strain induced in (In,Fe)Sb by choosing appropriate buffer layers.

Then, we characterized the magnetic properties of the (In,Fe)Sb thin films using magnetic circular dichroism (MCD) spectroscopy and superconducting quantum interference device (SQUID) magnetometry. To confirm that the ferromagnetism in the samples arises only from (In,Fe)Sb,
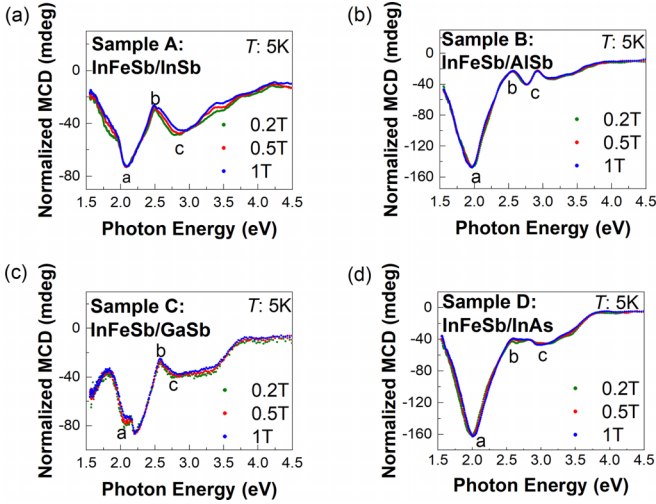
FIG. 3. Normalized MCD spectra (scaled to MCD intensity values at 1 T) of the four samples of (In,Fe)Sb grown on different buffers, measured at 5 K under various magnetic fields (0.2, 0.5, and 1 T) applied perpendicular to film plane.

we measured the MCD spectra of the samples. The MCD intensity can be expressed as $(90/\pi)[(R_+ - R_-)/(R_+ + R_-)] \propto \Delta E(1/R)(dR/dE)$, where R is the reflectivity and R_+ and R_- are the reflectivities for right (σ^+) and left (σ^-) circularly polarized light, respectively, E is the photon energy, and ΔE is the Zeeman splitting energy which is proportional to the magnetization M. As the MCD intensity is $\propto \Delta E(1/R)(dR/dE)$, it probes the spin-polarized band structure of the material. The MCD spectrum of an intrinsic ferromagnetic semiconductor is expected to show the spectral features of the host material along with enhanced peaks at critical points (optical energies). On the other hand, the MCD results of a semiconductor with second-phase metallic precipitates typically show a broad spectrum without any particular strongly enhanced peaks at the critical optical energies of the host material. The MCD spectra (at 5 K) are normalized by their intensity at E_1 ($\sim 1.96 - 2.20$ eV) of the samples. Next, as shown in Fig. 3, these normalized plots are scaled to the MCD intensity values at 1 T (for all samples). The normalized MCD spectra measured under different magnetic fields (0.2, 0.5, and 1 T) almost completely overlap on one spectrum in the whole photon-energy range, indicating that the MCD spectra come from the intrinsic (In,Fe)Sb and not from second-phase precipitations. This is because magnetization of a second ferromagnetic phase, if any, would respond to the magnetic field differently from that of (In,Fe)Sb. We also see a good agreement in the normalized *MCD–H* characteristics measured at three photon energies [a ($E_1 = 1.96 - 2.09$ eV), b ($E_1 + \Delta_1 = 2.5$ eV), and c ($2.76 - 3$ eV)] shown in Fig. S2 of Supplemental Material [55]. The slight deviations in the spectra may be due to local nanoscale Fe concentration fluctuations in the ferromagnetic (In,Fe)Sb layer, which are induced by spinodal decomposition. MCD spectra confirmed the single-phase intrinsic ferromagnetism of $(In_{0.85},Fe_{0.15})Sb$ in all the samples.

SQUID magnetometry was utilized to estimate the Curie temperature (T_C) as well as to obtain saturation magnetization
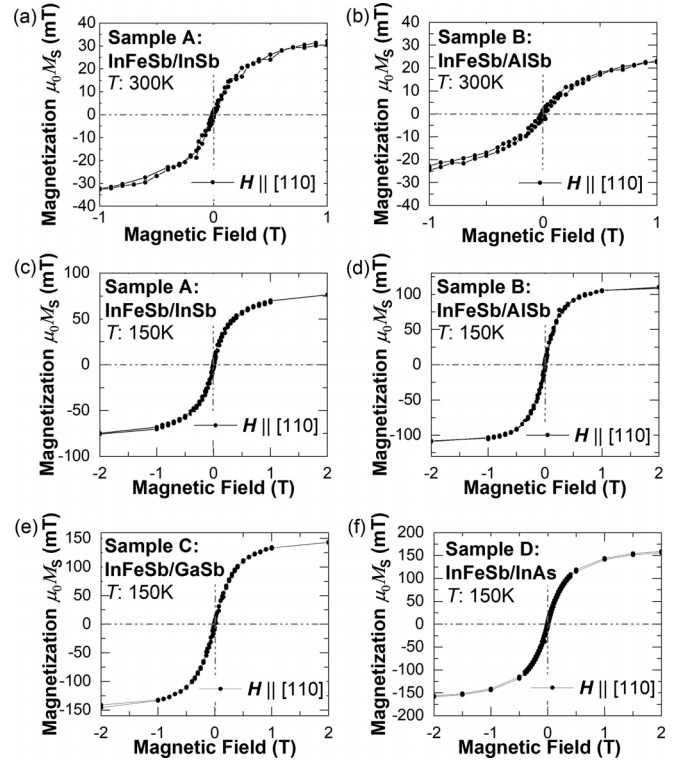

FIG. 4. Magnetization vs magnetic field (*M–H*) curves for samples A–D. (a), (b) *M–H* curves for samples A and B measured at 300 K. (c)–(f) *M–H* curves for samples A–D measured at 150 K. Magnetic field is applied along [110] direction in the film plane of the sample. From these data, saturation magnetization values are extracted to estimate magnetic anisotropy constants.

(M_S) values of all samples. From the temperature dependence of magnetization (*M−T* curves) described in Sec. 4 in Supplemental Material [55], the T_C for all the samples was estimated by Curie-Weiss plots. These results confirmed the ferromagnetic order at room temperature in the (In,Fe)Sb thin films of samples A and B, whereas for samples C and D, T_C was found to be lower than room temperature ($260 - 270$ K). The saturation magnetization values of the samples were extracted from the magnetic field dependence of magnetization (*M–H*) curves of $(In_{0.85},Fe_{0.15})Sb$ at 300 and 150 K, with the magnetic field ***H*** applied along the in-plane [110] axis (black solid circles), as shown in Fig. 4. We will use the saturation magnetization values measured in all the samples later for the estimation of the magnetic anisotropy constants at both 300 and 150 K.

III. METHODOLOGY AND FITTING MODEL

We performed FMR measurements using a JEOL electron spin-resonance spectrometer. For our measurements, we used 3 mm × 1 mm samples, with the [$\bar{1}$10] direction along the longer side and the [110] direction along the shorter side. Then, we put the sample on a quartz rod and placed it at the center of the microwave cavity where the TE_{011} resonance mode exists with a microwave frequency of 9.134 GHz. In our FMR measurements, a magnetic field (*h*) of the microwave radio frequency (rf) was applied along the [$\bar{1}$10] direction. The
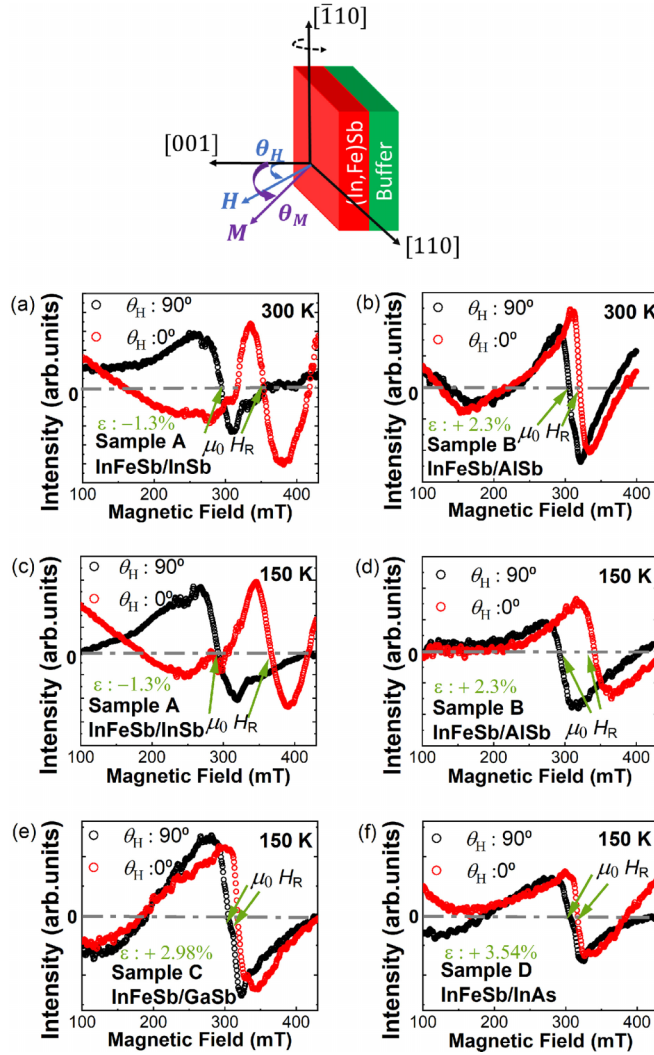
FIG. 5. Ferromagnetic resonance (FMR) spectra of $(In_{0.85},Fe_{0.15})Sb$ thin films grown on (a) InSb (sample A) and (b) AlSb (sample B) at 300 K. FMR spectra of $(In_{0.85},Fe_{0.15})Sb$ thin films grown on (c) InSb (sample A), (d) AlSb (sample B), (e) GaSb (sample C), and (f) InAs (sample D) at 150 K. Top view shows applied magnetic field (H) and magnetization (M) directions and definitions of their angles (θ_H and θ_M) used in Eqs. (4) and (5).

direction of the dc magnetic field H was rotated from the [001] to the [110] axis and defined by θ_H, which is the angle of H with respect to the [001] axis (that is perpendicular to the film plane). The crystallographic axes of the sample are illustrated in the inset in Fig. 5. We then measured FMR signals by sweeping the dc magnetic field H from 0 to 0.5 T and obtained the first derivative of the microwave absorption spectrum. We note that FMR peaks were superimposed by background signals, which were detected by performing FMR measurement without any sample on a quartz rod. These background signals were later subtracted from the raw data [52]. For magnetic anisotropy measurements, we rotated H from the in-plane direction (H//[110], $\theta_H = 90°$) to the perpendicular direction (H//[001], $\theta_H = 0°$). Since samples C and D did not show ferromagnetic behavior at 300 K, only the FMR measurement results at 150 K are shown in this study. All the measurements

were carried out with a microwave power of 200 mW at 300 and 150 K.

We used the derivatives of Lorentzian curves to obtain the resonant field $\mu_0 H_R$. As for the fitting of the curves of the angular dependence of $\mu_0 H_R$, we used the following equations as in the case of (Ga,Fe)Sb [52]:

$$E = E_{eff} + E_{Zeeman} = -K_{eff} \cos^2 \theta_M - M_S \mu_0 H \cos(\theta_H - \theta_M),$$
(1)

Here, E denotes the free-energy density of the material comprising the effective magnetic anisotropic energy E_{eff} and Zeeman energy E_{Zeeman}, μ_0 is the vacuum permeability constant, M_S is the saturation magnetization, and θ_M is the out-of-plane magnetization angle (angle between the magnetization and the [001] axis of the sample). E_{eff} is defined as the sum of the magnetocrystalline (E_i) anisotropy and shape (E_{sh}) magnetic anisotropy energy ($E_{eff} = E_i + E_{sh}$). Then, we define

$$K_{sh} = -\tfrac{1}{2}\mu_0 M_S^2,$$
(2)

$$K_i = \frac{\mu_0 M_S H_i}{2}, \text{ where } M_{eff} = M_S - H_i.$$
(3)

Here, H_i and M_{eff} represent the magnetocrystalline anisotropy field and the effective magnetization, respectively. Thus, K_i, K_{sh}, and K_{eff} (= $K_i + K_{sh}$) are the magnetic anisotropy constants corresponding to E_i, E_{sh}, and E_{eff}, respectively. By definition, a positive value for the constants indicates preference for perpendicular magnetization and a negative value indicates preference for in-plane magnetization [61,62].

The fitting equations for the angular dependence of the resonant field are given as

$$\left(\frac{\omega}{\gamma}\right)^2 = [\mu_0 H_R \cos(\theta_H - \theta_M) - \mu_0(M_S - H_i)\cos^2(\theta_M)]$$

$$\times [\mu_0 H_R \cos(\theta_H - \theta_M) - \mu_0(M_S - H_i)\cos(2\theta_M)],$$
(4)

$$\mu_0 H_R = \frac{\mu_0(M_S - H_i)\sin(2\theta_M)}{2\sin(\theta_M - \theta_H)},$$
(5)

where ω, γ, and $\mu_0 H_R$ stand for the angular frequency of magnetization precession, the gyromagnetic ratio, and the resonance field, respectively.

Equations (4) and (5) are obtained by subjecting the free-energy density E of the material [Eq. (1)] to the Smit-Beljers' relation [63,64] and resonance conditions ($\partial E/\partial\theta_M = 0$; $\partial E/\partial\phi_M = 0$; ϕ_M denotes the in-plane magnetization angle which is not used here). Here, the g factor is included in the γ term, which stands for the gyromagnetic ratio ($\gamma = g\mu_B/\hbar$), where μ_B and $\hbar$ are the Bohr magneton and the reduced Planck's constant, respectively. We assumed that E_i depends only on the out-of-plane magnetic field angle (θ_H), because the in-plane magnetic field angle (ϕ_H) dependence of FMR was nearly isotropic in all the samples. From the data curves and fitting Eqs. (4) and (5), we obtained the fitting parameters M_{eff} and g. These are used in finding the values of θ_M and $\mu_0 H_R$. Saturation magnetization (M_S) values were obtained from the SQUID measurements (Fig. 4) and the anisotropy constants K_i, K_{sh}, and K_{eff} were estimated.
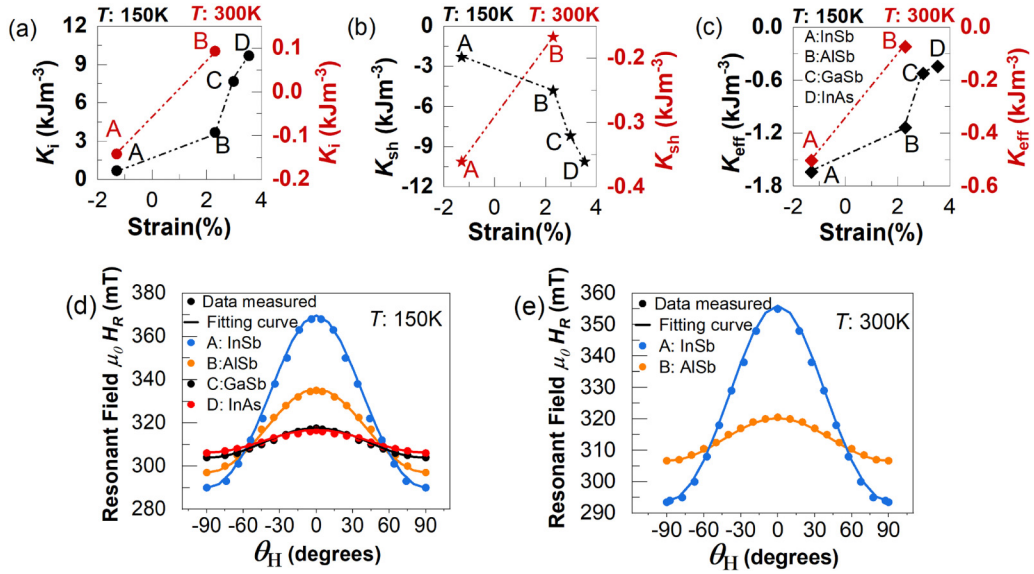
FIG. 6. Effect of epitaxial strain on magnetic anisotropy constants: (a) Magnetocrystalline anisotropy constant K_i, (b) shape anisotropy constant K_{sh}, and (c) effective magnetic anisotropy constant K_{eff} ($= K_i + K_{sh}$) estimated from data at 150 K (black, left axis) and 300 K (red, right axis). (d), (e) Dependence of resonant magnetic field $\mu_0 H_R$ on θ_H.

IV. RESULTS

The FMR spectra of (In,Fe)Sb in samples A–D are shown in Figs. 5(a)–5(f). The measurements were carried out at 300 and 150 K. Here, $\theta_H = 0°$ and $90°$ correspond to the cases of **H**//[001] (perpendicular) and **H**//[110] (in plane), respectively. In n-type FMSs, the observation of FMR has never been reported at room temperature (300 K). In all the samples, the resonant magnetic field $\mu_0 H_R$ was smaller in magnitude when $\theta_H = 90°$ than when $\theta_H = 0°$, indicating that the magnetization easy axis is in-plane in all the samples. However, we see that the difference $\Delta(\mu_0 H_R)$ in $\mu_0 H_R$ between $\theta_H = 0°$ and $90°$ varied largely between the samples as shown in Fig. 5. This suggests that magnetocrystalline anisotropy is affected by the epitaxial strain effect induced in the (In,Fe)Sb layer by its buffer layer underneath. We clearly observed that sample A, where a tensile strain is applied to (In,Fe)Sb, shows the largest $\Delta(\mu_0 H_R)$. By driving the strain towards compressive strain from sample A to D, $\Delta(\mu_0 H_R)$ is reduced by about 7.6 times; $\Delta(\mu_0 H_R)$ is 78 mT in sample A and 10.25 mT in sample D, as shown in Fig. 6(d).

Table I and II show the saturation magnetization (M_S), anisotropy field (H_i), effective magnetization (M_{eff}), and g-factor values obtained from the fitting of FMR angular-dependence curves at 300 and 150 K, respectively. The anisotropy constants K_i, K_{sh}, and K_{eff} are estimated from

Eqs. (2) and (3). The trends of these constants for all the samples at 150 K are shown in Figs. 6(a)–6(c). We found that K_{eff} in all the samples were negative (by definition of the equation in our model) as shown in Fig. 6(c), indicating the preference for in-plane magnetization. However, as the compressive strain was increased, the magnetocrystalline anisotropy constant K_i became larger in magnitude as shown in Fig. 6(a). This implies that the compressive strain induces the preference for perpendicular magnetization. This is also evident from the anisotropy field values (H_i) given in Table II, indicating that as the in-plane compressive strain on the ferromagnetic film increases, the magnitude B of H_i increases. It is important to note that at 150 K, the negative K_{sh} had a much larger magnitude than K_i, resulting in the net magnetic anisotropy of in-plane in nature, as clearly illustrated by the negative values of K_{eff} in Fig. 6(c). At 300 K, on the other hand, the magnetocrystalline anisotropy constant K_i showed a sign change from positive to negative [shown in Fig. 6(a)] when we changed the epitaxial strain induced in (In,Fe)Sb from compressive (AlSb buffer) to tensile (InSb buffer) strain. However, K_{eff} values are negative in Fig. 6(c), indicating that the net preference for the direction of magnetization is still in plane for both samples. This is because the contribution

TABLE I. Parameters used in analysis of angular dependence of FMR at 300 K: Strain ε (%), saturation magnetization ($\mu_0 M_S$), effective magnetization ($\mu_0 M_{eff}$), anisotropy field ($\mu_0 H_i$), and g factor.

Sample, buffer layer	Strain ε (%)	$\mu_0 M_S$ (mT)	$\mu_0 M_{eff}$ (mT)	$\mu_0 H_i$ (mT)	g factor
(A) InSb	−1.3	30.14	42	−11.86	2.081 ± 0.003
(B) AlSb	+2.3	20.51	9.1	+11.41	2.101 ± 0.003

TABLE II. Parameters used in analysis of angular dependence of FMR at 150 K: Strain ε (%), saturation magnetization ($\mu_0 M_S$), effective magnetization ($\mu_0 M_{eff}$), anisotropy field ($\mu_0 H_i$), and g factor.

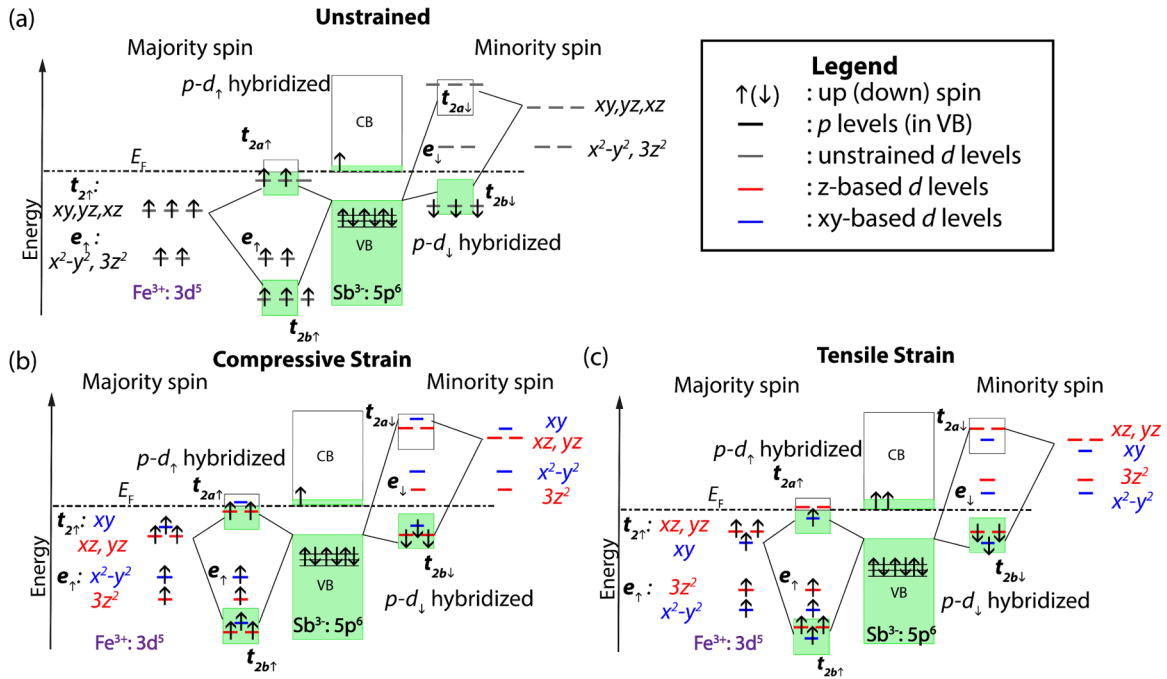| Sample, buffer layer	Strain ε (%)	$\mu_0 M_S$ (mT)	$\mu_0 M_{eff}$ (mT)	$\mu_0 H_i$ (mT)	g factor
(A) InSb	−1.3	76.34	54	+22.34	2.07 ± 0.001
(B) AlSb	+2.3	109.99	26	+83.99	2.11 ± 0.001
(C) GaSb	+2.98	143.55	9.2	+134.35	2.115 ± 0.001
(D) InAs	+3.54	158.91	7	+151.91	2.11 ± 0.002

FIG. 7. Schematic illustration of distribution of electrons (spins) in different d orbitals for differently strained (In,Fe)Sb samples. CB and VB denote the conduction band and valence band of (In,Fe)Sb. Dotted line is the Fermi-level (E_F) position assumed in this model. t_2 (d) orbitals from Fe hybridize with Sb ligand p orbitals forming antibonding (a) and bonding (b) states. Even after hybridization, we expect energy differences within t_2 levels to persist in antibonding (t_{2a}) and bonding states (t_{2b}). (a) Electron distribution and energy levels of d orbitals in unstrained case. (b), (c) Electron distribution and d-orbital energy levels in compressive and tensile strain cases of (In,Fe)Sb. Effect of strain causes distortion in energy levels of the t_2 and e orbitals. Difference in electron occupation of $t_{2a\uparrow}$ between compressive- and tensile-strained (In,Fe)Sb thin films causes preference of K_i for perpendicular and in-plane magnetic anisotropy, respectively. This may also cause different electron (spin) occupation in the conduction band, leading to different magnetic moment per Fe atom.

of shape anisotropy, which induces in-plane magnetization, is stronger than the magnetocrystalline anisotropy. The magnitude of the shape anisotropy constant is always larger in magnitude than the magnetocrystalline component, as shown in Figs. 6(a) and 6(b).

V. DISCUSSION

From the results described above, it is found that the application of compressive strain to the ferromagnetic (In,Fe)Sb film results in the preference of K_i for perpendicular magnetization. This is clearly indicated by the increasing positive values of the magnetocrystalline anisotropy constant K_i with increasing compressive strain [Fig. 6(a)]. This preference is reduced or changed to in-plane magnetization upon changing the strain towards tensile. The magnetocrystalline anisotropy is generally attributed to spin-orbit interaction, which couples the spin moments to the anisotropy from the orbital moments [65,66]. The dependence of the easy-magnetization axis on the strain thus may be attributed to the change in orbital moment anisotropy of the occupied d orbitals, as we will discuss hereafter. In our discussion, we denote the z axis along the [001] direction of the sample and x- and y axes along the in-plane directions. We consider that if electrons occupy d orbitals having a z component, their spins are likely to favor the z direction (perpendicular magnetization), as observed in the case of Co [67]. Similarly, the in-plane spin direction is energetically favorable when the

electrons occupy xy-based d orbitals. The easy-magnetization direction is then determined by the competition between the in-plane ($m_0^{\parallel}$) and perpendicular ($m_0^{\perp}$) spin moments, which is quantified as the magnetocrystalline energy $\Delta_{so} \propto (m_0^{\perp} - m_0^{\parallel})$ [66,67]. In the case of (In,Fe)Sb, the ferromagnetic behavior is largely governed by short-range magnetic couplings between Fe spins in Fe-rich domains [23], particularly the interaction of the second-nearest Fe^{3+} moments [68] (distance around 1.5 times the lattice constant of the material).

It is also important to note that most of the Fe atoms should be in the isoelectronic Fe^{3+} states. Under a tetrahedral crystal field as shown by Fig. 7(a), the d orbitals [69,70] split into triply degenerate t orbitals ($3d_{xy}$, $3d_{yz}$, $3d_{xz}$), which are higher in energy, and doubly degenerate e orbitals ($3d_{3z^2}$, $3d_{x^2-y^2}$). Upon the application of strain, we expect that the degenerate d and e orbitals also split in energy because of the Jahn-Teller effect, as schematically shown in Figs. 7(b) and 7(c). An in-plane compressive strain induces tensile strain in its perpendicular direction, thus reducing the interaction of the z-based d orbitals of the neighboring Fe atoms (along the perpendicular direction). This causes the lowering of the $3d_{xy}$, $3d_{yz}$, $3d_{xz}$ energy levels as shown in Fig. 7(b). On the other hand, the energy of the xy-based d orbitals is lowered for the case of the samples with in-plane tensile strain as shown by Fig. 7(c). Upon hybridization with the p ligands of Sb, the t_2 levels form antibonding and bonding states. Meanwhile,

the e levels do not hybridize with the Sb ligands because of incompatibility of symmetry. In our model, we expect that the Fermi level lies in the Fe-impurity band that is close to the conduction-band bottom, resulting in partial occupation of electrons in the majority-spin antibonding band ($t_{2a\uparrow}$) and the conduction-band bottom. As shown in Figs. 7(b) and 7(c), depending on the type of strain, majority-spin electrons occupy different types of d orbitals near the Fermi level: In compressive strain, majority-spin electrons occupy the z-based (xz and yz) d orbitals, while in tensile strain they occupy the xy-based orbitals. Also, for the charge-neutrality condition to hold, the number of electrons occupying the conduction-band bottom changes correspondingly. This may be the reason why we do not observe a perfect 5 μ_B magnetic moment in compressive (3.2 μ_B) or tensile (2.6 μ_B) strain samples. We note that the contribution to the magnetic anisotropy of the s-orbital electrons occupying the conduction band, which is mostly isotropic, is small. Therefore, under compressive strain the electrons in the z-based orbital moments have dominant contribution, resulting in $\Delta_{SO} > 0$, favoring perpendicular magnetization, whereas for tensile strain the electrons in the xy-based orbital moments have larger contribution, thus exhibiting preference for in-plane magnetization. Therefore, our microscopic scenario can explain how strain modifies the preference for magnetization directions.

Finally, we note that the strain dependence of the magnetic anisotropy in (In,Fe)Sb is similar to that in (Ga,Fe)Sb [52] but opposite to that in (Ga,Mn)As [44]. When we compare the magnetic anisotropy in the Fe-doped and the Mn-doped FMSs, there are two main differences: (i) The magnitude of the magnetocrystalline anisotropy constant K_i of (Ga,Mn)As is much larger [44], about 40 times than that of the Fe-doped FMSs. (ii) On changing the strain from tensile to compressive, the change in K_i favors in-plane magnetization in (Ga,Mn)As [44] but perpendicular magnetization in (In,Fe)Sb and (Ga,Fe)Sb. To explain these different trends, it is important to understand the electronic configurations of the Mn-doped and Fe-doped FMSs. The Mn dopant in (Ga,Mn)As plays the role of both a localized magnetic moment and an acceptor, supplying a hole that is weakly bound to the Mn atom. As a result, the Mn ions do not exhibit a pure Mn^{2+} ([Ar] $4s^0 3d^5$) state but rather a mixed state of Mn^{2+} and Mn^{3+}, where the Mn^{3+} comprises a Mn^{2+} ion and a ligand hole ($\underline{L}$), that is $3d^5\underline{L}$, as confirmed experimentally in Ref. [71]. The total orbital angular momentum L of such a Mn^{3+} ($3d^5$ + hole) deviates largely from zero ($L = 0$ for a pure $3d^5$ configuration). On the other hand, in Fe-doped FMSs, Fe atoms mainly substitute the group-III atoms in the Fe^{3+} state with the [Ar] $4s^0 3d^5$ electronic configuration and supply no carrier. Thus, the orbital angular momentum $\boldsymbol{L}$ of the Fe ions is much smaller than that of the Mn ions, resulting in a smaller atomic spin-orbit interaction ($\propto \lambda \boldsymbol{L} \cdot \boldsymbol{S}$, where λ is the spin-orbit coupling constant and $\boldsymbol{S}$ is the spin angular momentum) in the Fe-doped FMSs than in the Mn-doped FMSs. This may explain why the K_i values

of (Ga,Mn)As are much larger than that in the Fe-doped FMSs.

Furthermore, the opposite dependence of K_i on the strain in the Mn- and Fe-doped FMSs can be attributed to different signs of λ in the Mn- and Fe-doped FMSs. Based on the above discussion of (Ga,Mn)As, the $3d^5\underline{L}$ configuration can be considered as an electronic configuration between $3d^4$ and $3d^5$, which means that orbital angular momentum L of Mn is not zero. The configuration can be assumed to be $3d^{5-x}$ where $0 < x < 1$. Theoretically, the signs of the spin-orbit interaction constant for transition-metal ions in $3d^{5-x}$ (as for Mn^{2+} and Mn^{3+} states described above) and $3d^6$ (which is the case of Fe^{2+}) configurations are positive and negative, respectively [72]. Considering that there is also a certain amount of Fe in the Fe^{2+} states ($3d^6$ configuration) in the Fe-doped FMSs [73], the opposite signs of the spin-orbit interaction constants of the Mn^{3+}(described here) and Fe^{2+} ions may result in the opposite trends of K_i observed in the Mn- and Fe-doped FMSs. Future studies are definitely required to fully understand the underlying mechanism of the magnetic anisotropy in these FMSs.

VI. CONCLUSION

This study presents the observation of ferromagnetic resonance in n-type ferromagnetic semiconductors and clarifies the strain-dependent magnetic anisotropy of (In,Fe)Sb thin films. Ferromagnetic semiconductor $(In_{0.85},Fe_{0.15})$Sb thin films (15 nm thick) were grown by LT-MBE on different buffer layers (InSb, AlSb, GaSb, and InAs), which induce different strains ranging from +3.54% (InAs: compressive) to −1.3% (InSb: tensile). From the ferromagnetic resonance measurements at both 300 and 150 K, we found that by changing the epitaxial strain induced in the (In,Fe)Sb films from compressive to tensile, the magnetocrystalline anisotropy constant (K_i) can be changed; the magnetization direction preference is changed from perpendicular to in-plane. At both temperatures, the magnitude of the shape anisotropy constant (K_{sh}) is larger than K_i, and thus the effective magnetic anisotropy and easy-magnetization axis are in plane in all the samples. Furthermore, we discussed a possible origin of such strain-dependent magnetic anisotropy in Fe-doped III-V ferromagnetic semiconductors based on a band-structure model with $p - d$ hybridization.

[1] H. Ohno, Properties of ferromagnetic III–V semiconductors, J. Magn. Magn. Mater. **200**, 110 (1999).

[2] M. Tanaka, S. Ohya, and P. N. Hai, Recent progress in III-V based ferromagnetic semiconductors: Band structure, Fermi level, and tunneling transport, Appl. Phys. Rev. **1**, 011102 (2014).

[3] T. Dietl and H. Ohno, Dilute ferromagnetic semiconductors: Physics and spintronic structures, Rev. Mod. Phys. **86**, 187 (2014).

[4] G. Schmidt, D. Ferrand, L. W. Molenkamp, A. T. Filip, and B. J. van Wees, Fundamental obstacle for electrical spin injection from a ferromagnetic metal into a diffusive semiconductor, Phys. Rev. B **62**, R4790(R) (2000).

[5] S. Sato, M. Tanaka, and R. Nakane, Spin transport in Si-based spin metal-oxide-semiconductor field-effect transistors: Spin drift effect in the inversion channel and spin relaxation in the n+− Si source/drain regions, Phys. Rev. B **102**, 035305 (2020).

[6] H. Ohno, A. Shen, F. Matsukura, A. Oiwa, A. Endo, S. Katsumoto, and Y. Iye, "(Ga, Mn) As: A new diluted magnetic semiconductor based on GaAs, Appl. Phys. Lett. **69**, 363 (1996).

[7] T. Hayashi, M. Tanaka, T. Nishinaga, H. Shimada, H. Tsuchiya, and Y. Otuka, (Ga, Mn) As: GaAs-based III–V diluted magnetic semiconductors grown by molecular beam epitaxy, J. Cryst. Growth **175**, 1063 (1997).

[8] A. Van Esch, L. Van Bockstal, J. De Boeck, G. Verbanck, A. S. van Steenbergen, P. J. Wellmann, B. Grietens, R. Bogaerts, F. Herlach, and G. Borghs, Interplay between the magnetic and transport properties in the III-V diluted magnetic semiconductor $Ga_{1-x}Mn_x$ As, Phys. Rev. B **56**, 13103 (1997).

[9] M. Kohda, Y. Ohno, K. Takamura, F. Matsukura, and H. Ohno, A spin Esaki diode, Jpn. J. Appl. Phys. **40**, L1274 (2001).

[10] T. Arakawa, J. Shiogai, M. Maeda, M. Ciorga, M. Utz, D. Schuh, Y. Niimi, M. Kohda, J. Nitta, D. Bougeard, D. Weiss, and K. Kobayashi, Tunneling mechanism in a (Ga, Mn) As/GaAs-based spin Esaki diode investigated by bias-dependent shot noise measurements, Phys. Rev. B **102**, 045308 (2020).

[11] M. Tanaka and Y. Higo, Large Tunneling Magnetoresistance in GaMnAs/AlAs/GaMnAs Ferromagnetic Semiconductor Tunnel Junctions, Phys. Rev. Lett. **87**, 026602 (2001).

[12] S. Ohya, P. N. Hai, Y. Mizuno, and M. Tanaka, Quantum size effect and tunneling magnetoresistance in ferromagnetic-semiconductor quantum heterostructures, Phys. Rev. B **75**, 155328 (2007).

[13] H. X. Tang, R. K. Kawakami, D. D. Awschalom, and M. L. Roukes, Giant Planar Hall Effect in Epitaxial (Ga, Mn) As Devices, Phys. Rev. Lett. **90**, 107201 (2003).

[14] L. Chen, F. Matsukura, and H. Ohno, Direct-current voltages in (Ga, Mn) As structures induced by ferromagnetic resonance, Nat. Commun. **4**, 2055 (2013).

[15] S. Ghosh and P. Bhattacharya, Electrical spin injection into $In_{0.4}Ga_{0.6}As$/GaAs quantum dots using (Ga, Mn) As., J. Vac. Sci. Technol. B **20**, 1182 (2002).

[16] M. Oestreich, Injecting spin into electronics, Nature (London) **402**, 735 (1999).

[17] Y. Ohno, D. K. Young, B. Beschoten, F. Matsukura, H. Ohno, and D. D. Awschalom, Electrical spin injection in a ferromagnetic semiconductor heterostructure, Nature (London) **402**, 790 (1999).

[18] Y. Chye, M. E. White, E. Johnston-Halperin, B. D. Gerardot, D. D. Awschalom, and P. M. Petroff, Spin injection from (Ga, Mn) As into InAs quantum dots, Phys. Rev. B **66**, 201301 (2002).

[19] T. Schallenberg and H. Munekata, Preparation of ferromagnetic (In, Mn) As with a high Curie temperature of 90 K, Appl. Phys. Lett. **89**, 042507 (2006).

[20] L. Chen, X. Yang, F. Yang, J. Zhao, J. Misuraca, P. Xiong, and S. von Molnar, Enhancing the Curie temperature of ferromagnetic semiconductor (Ga, Mn) As to 200 K via nanostructure engineering, Nano Lett. **11**, 2584 (2011).

[21] N. T. Tu, P. N. Hai, L. D. Anh, and M. Tanaka, Magnetic properties and intrinsic ferromagnetism in (Ga, Fe) Sb ferromagnetic semiconductors, Phys. Rev. B **92**, 144403 (2015).

[22] N. T. Tu, P. N. Hai, L. D. Anh, and M. Tanaka, High-temperature ferromagnetism in heavily Fe-doped ferromagnetic semiconductor (Ga, Fe) Sb, Appl. Phys. Lett. **108**, 192401 (2016).

[23] N. T. Tu, P. N. Hai, L. D. Anh, and M. Tanaka, Electrical control of ferromagnetism in the n-type ferromagnetic semiconductor (In, Fe) Sb with high Curie temperature, Appl. Phys. Lett. **112**, 122409 (2018).

[24] V. P. Lesnikov, M. V. Ved', O. V. Vikhrova, Y. A. Danilov, B. N. Zvonkov, A. V. Zdoroveyshchev, I. L. Kalentyeva, A. V. Kudrin, and R. N. Kryukov, Diode heterostructures with narrow-gap ferromagnetic $A^3 FeB^5$ semiconductors of various conduction type, Phys. Solid State **63**, 1028 (2021).

[25] A. V. Kudrin, Yu. A. Danilov, V. P. Lesnikov, and E. A. Pitirimova, Nonlinear room-temperature Hall effect in n-InFeAs layers, Phys. Lett. **42**, 88 (2016).

[26] A. V. Kudrin, Yu. A. Danilov, V. P. Lesnikov, M. V. Dorokhin, O. V. Vikhrova, D. A. Pavlov, Y. V. Usov, I. N. Antonov, R. N. Kriukov, A. V. Alaferdov, and N. A. Sobolev, High-temperature intrinsic ferromagnetism in the (In, Fe) Sb semiconductor, J. Appl. Phys. **122**, 183901 (2017).

[27] A. V. Kudrin, V. P. Lesnikov, D. A. Pavlov, Yu. V. Usov, Yu. A. Danilov, M. V. Dorokhin, O. V. Vikhrova, V. E. Milin, R. N. Kriukov, Yu. M. Kuznetsov, V. N. Trushin, and N. A. Sobolev, Formation of epitaxial pin structures on the basis of (In, Fe) Sb and (Ga, Fe) Sb diluted magnetic semiconductors layers, J. Magn. Magn. Mater. **487**, 165321 (2019).

[28] L. D. Anh, D. Kaneko, P. N. Hai, and M. Tanaka, Growth and characterization of insulating ferromagnetic semiconductor (Al, Fe) Sb, Appl. Phys. Lett. **107**, 232405 (2015).

[29] N. T. Tu, P. N. Hai, L. D. Anh, and M. Tanaka, Heavily Fe-doped ferromagnetic semiconductor (In, Fe) Sb with high Curie temperature and large magnetic anisotropy, Appl. Phys. Express **12**, 103004 (2019).

[30] P. N. Hai, L. D. Anh, S. Mohan, T. Tamegai, M. Kodzuka, T. Ohkubo, K. Hono, and M. Tanaka, Growth and characterization of n-type electron-induced ferromagnetic semiconductor (In, Fe) As, Appl. Phys. Lett. **101**, 182403 (2012).

[31] L. D. Anh, P. N. Hai, and M. Tanaka, Observation of spontaneous spin-splitting in the band structure of an n-type zinc-blende ferromagnetic semiconductor, Nat. Commun. **7**, 13810 (2016).

[32] K. Takiguchi, L. D. Anh, T. Chiba, T. Koyama, D. Chiba, and M. Tanaka, Giant gate-controlled proximity magnetoresistance in semiconductor-based ferromagnetic–non-magnetic bilayers, Nat. Phys. **15**, 1134 (2019).

[33] P. N. Hai, M. Yoshida, A. Nagamine, and M. Tanaka, Inhomogeneity-induced high temperature ferromagnetism in n-type ferromagnetic semiconductor (In, Fe) As grown on vicinal GaAs substrates, Jpn. J. Appl. Phys. **59**, 063002 (2020).

[34] T. Miyazaki and N. Tezuka, Giant magnetic tunneling effect in Fe/Al$_2$O$_3$/Fe junction, J. Magn. Magn. Mater. **139**, L231 (1995).

[35] J. S. Moodera, L. R. Kinder, T. M. Wong, and R. Meservey, Large Magnetoresistance at Room Temperature in Ferromagnetic Thin Film Tunnel Junctions, Phys. Rev. Lett. **74**, 3273 (1995).

[36] H. X. Wei, Q. H. Qin, M. Ma, R. Sharif, and X. F. Han, 80% tunneling magnetoresistance at room temperature for thin Al–O barrier magnetic tunnel junction with CoFeB as free and reference layers, J. Appl. Phys. **101**, 09B501 (2007).

[37] I. Žutić, J. Fabian, and S. Das Sarma, Spintronics: Fundamentals and applications, Rev Mod. Phys. **76**, 323 (2004).

[38] A. A. Khudorozhkov, P. N. Skirdkov, K. A. Zvezdin, P. M. Vetoshko, and A. F. Popkov, Spin-torque diode frequency tuning via soft exchange pinning of both magnetic layers, Phys. Rev. B **96**, 214410 (2017).

[39] L. D. Anh, P. N. Hai, and M. Tanaka, Electrical tuning of the band alignment and magnetoconductance in an n-type ferromagnetic semiconductor (In, Fe) As-based spin-Esaki diode, Appl. Phys. Lett. **112**, 102402 (2018).

[40] S. Datta and B. Das, Electronic analog of the electro-optic modulator, Appl. Phys. Lett. **56**, 665 (1990).

[41] S. Sugahara and M. Tanaka, A spin metal–oxide–semiconductor field-effect transistor using half-metallic-ferromagnet contacts for the source and drain, Appl. Phys. Lett. **84**, 2307 (2004).

[42] U. Welp, V. K. Vlasko-Vlasov, A. Menzel, H. D. You, X. Liu, J. K. Furdyna, and T. Wojtowicz, Uniaxial in-plane magnetic anisotropy of Ga$_{1-x}$Mn$_x$As, Appl. Phys. Lett. **85**, 260 (2004).

[43] X. Liu, W. L. Lim, M. Dobrowolska, J. K. Furdyna, and T. Wojtowicz, Ferromagnetic resonance study of the free-hole contribution to magnetization and magnetic anisotropy in modulation-doped Ga$_{1-x}$Mn$_x$As/Ga$_{1-y}$Al$_y$As: Be, Phys. Rev. B **71**, 035307 (2005).

[44] X. Liu, Y. Sasaki, and J. K. Furdyna, Ferromagnetic resonance in Ga$_{1-x}$Mn$_x$As: Effects of magnetic anisotropy, Phys. Rev. B **67**, 205204 (2003).

[45] D. Y. Shin, S. J. Chung, Sanghoon Lee, X. Liu, and J. K. Furdyna, Temperature dependence of magnetic anisotropy in ferromagnetic (Ga, Mn) As films: Investigation by the planar Hall effect, Phys. Rev. B **76**, 035327 (2007).

[46] H. Son, S. Chung, S.-Y. Yea, S. Lee, X. Liu, and J. K. Furdyna, Quantitative investigation of the magnetic anisotropy in GaMnAs film by using Hall measurement, J. Appl. Phys. **103**, 07F313 (2008).

[47] S. Kim, H. Lee, T. Yoo, S. Lee, S. Lee, X. Liu, and J. K. Furdyna, Mapping of magnetic anisotropy in strained ferromagnetic semiconductor GaMnAs films, J. Appl. Phys. **107**, 103911 (2010).

[48] H. Terada, S. Ohya, Y. Iwasa, and M. Tanaka, Magnetic anisotropy control by applying an electric field to the side surface of ferromagnetic films, Sci. Rep. **7**, 5618 (2017).

[49] A. Shen, F. Matsukura, Y. Sugawara, T. Kuroiwa, H. Ohno, A. Oiwa, A. Endo, S. Katsumoto, and Y. Iye, Epitaxy and properties of InMnAsAlGaSb diluted magnetic III–V semiconductor heterostructures, Appl. Surf. Sci. **113**, 183 (1997).

[50] P. T. Chiu, S. J. May, and B. W. Wessels, Origin of uniaxial magnetic anisotropy in epitaxial InMnAs thin films, J. Appl. Phys. **99**, 083907 (2006).

[51] D. Chiba, M. Sawicki, Y. Nishitani, Y. Nakatani, F. Matsukura, and H. Ohno, Magnetization vector manipulation by electric fields, Nature (London) **455**, 515 (2008).

[52] S. Goel, L. D. Anh, S. Ohya, and M. Tanaka, Ferromagnetic resonance and control of magnetic anisotropy by epitaxial strain in the ferromagnetic semiconductor (Ga$_{0.8}$, Fe$_{0.2}$) Sb at room temperature, Phys. Rev. B **99**, 014431 (2019).

[53] S. Goel, L. D. Anh, N. T. Tu, S. Ohya, and M. Tanaka, In-plane to perpendicular magnetic anisotropy switching in heavily-Fe-doped ferromagnetic semiconductor (Ga, Fe) Sb with high Curie temperature, Phys. Rev. Mater. **3**, 084417(2019).

[54] S. Goel, L. D. Anh, N. T. Tu, S. Ohya, and M. Tanaka, Temperature dependence of magnetic anisotropy in heavily Fe-doped ferromagnetic semiconductor (Ga, Fe) Sb, J. Appl. Phys. **127**, 023904 (2020).

[55] See Supplemental Material at http://link.aps.org/supplemental/10.1103/PhysRevB.108.014421 for additional descriptions and supplemental data, which include Refs. [56–60].

[56] G. Giesecke and H. Pfister, Precision determination of the lattice constants of III-V compounds, Acta Crystallogr. **11**, 369 (1958).

[57] R. Weil, Correction to the elastic constants of AlSb, J. Appl. Phys **43**, 4271 (1972).

[58] R. F. Potter, Elastic moduli of indium antimonide, Phys. Rev. **103**, 47 (1956).

[59] N. T. Tu, P. N. Hai, L. D. Anh, and M. Tanaka, High-temperature ferromagnetism in new n-type Fe-doped ferromagnetic semiconductor, (In, Fe) Sb, Appl. Phys. Express **11**, 063005 (2018).

[60] T. E. Hasty, Ferromagnetic resonance in multidomain thin films, J. Appl. Phys. **35**, 1434 (1964).

[61] M. Farle, Ferromagnetic resonance of ultrathin metallic layers, Rep. Prog. Phys. **61**, 755 (1998).

[62] M. T. Johnson, P. J. H. Bloemen, F. J. A. den Broeder, and J. J. de Vries, Magnetic anisotropy in metallic multilayers, Rep. Prog. Phys. **59**, 1409 (1996).

[63] J. Smit and H. G. Beljers, Ferromagnetic resonance absorption in BaFe$_{12}$O$_{19}$, a highly anisotropic crystal, Phillips Res. Rep. **10**, 113 (1955).

[64] X. Liu and J. K. Furdyna, Ferromagnetic resonance in Ga$_{1-x}$Mn$_x$As dilute magnetic semiconductors, J. Phys.: Condens. Matter **18**, R245(R) (2006).

[65] J. H. Van Vleck, On the anisotropy of cubic ferromagnetic crystals, Phys. Rev. **52**, 1178 (1937).

[66] P. Bruno, Tight-binding approach to the orbital magnetic moment and magnetocrystalline anisotropy of transition-metal monolayers, Phys. Rev. B **39**, 865 (1989).

[67] J. Stohr, Exploring the microscopic origin of magnetic anisotropies with X-ray magnetic circular dichroism (XMCD) spectroscopy, J. Magn. Magn. Mater. **200**, 470 (1999).

[68] H. Shinya, T. Fukushima, A. Masago, K. Sato, and H. Katayama-Yoshida, First-principles prediction of the control of magnetic properties in Fe-doped GaSb and InSb, J. Appl. Phys. **124**, 103902 (2018).

[69] S. Sakamoto, N. T. Tu, Y. Takeda, S.-I. Fujimori, P. N. Hai, L. D. Anh, Y. K. Wakabayashi, G. Shibata, M. Horio, K. Ikeda, Y. Saitoh, H. Yamagami, M. Tanaka, and A. Fujimori,

Electronic structure of the high$-T_C$ ferromagnetic semiconductor (Ga, Fe) Sb: X-ray magnetic circular dichroism and resonance photoemission spectroscopy studies, Phys. Rev. B **100**, 035204 (2019).

[70] T. Takeda, M. Suzuki, L. D. Anh, N. T. Tu, T. Schmitt, S. Yoshida, M. Sakano, K. Ishizaka, Y. Takeda, S.-I. Fujimori, M. Seki, H. Tabata, A. Fujimori, V. N. Strocov, M. Tanaka, and M. Kobayashi, Hybridization between the ligand p band and Fe$-$3 d orbitals in the p-type ferromagnetic semiconductor (Ga, Fe) Sb, Phys. Rev. B **101**, 155142 (2020).

[71] M. Kobayashi, H. Niwa, Y. Takeda, A. Fujimori, Y. Senba, H. Ohashi, A. Tanaka, S. Ohya, P. N. Hai, M. Tanaka, Y. Harada,

and M. Oshima, Electronic Excitations of a Magnetic Impurity State in the Diluted Magnetic Semiconductor (Ga, Mn) As, Phys. Rev. Lett. **112**, 107203 (2014).

[72] S. Koseki, N. Matsunaga, T. Asada, M. W. Schmidt, and M. S. Gordon, Spin–orbit coupling constants in atoms and ions of transition elements: Comparison of effective core potentials, model core potentials, and all-electron methods, J. Phys. Chem. A **123**, 2325 (2019).

[73] K. Sriharsha, L. D. Anh, N. T. Tu, S. Goel, and M. Tanaka, Magneto-optical spectra and the presence of an impurity band in p-type ferromagnetic semiconductor (Ga, Fe) Sb with high Curie temperature, APL Mater. **7**, 021105 (2019).